

Electrolyte design for reversible zinc metal chemistry

Received: 13 August 2024

Accepted: 19 December 2024

Published online: 02 January 2025



Bao Zhang^{1,2,8}, Jia Yao^{3,8}, Chao Wu^{4,5}, Yuanjian Li⁶, Jia Liu⁷, Jiaqi Wang¹, Tao Xiao², Tao Zhang^{1,2}, Daqian Cai², Jiawen Wu², Zhi Wei Seh⁶, Shibo Xi⁵, Hao Wang³, Wei Sun¹✉, Houzhao Wan³✉ & Hong Jin Fan²✉

Metal anodes hold significant promise for next-generation energy storage, yet achieving highly reversible plating/stripping remains challenging due to dendrite formation and side reactions. Here we present a tailored electrolyte design to surpass 99.9% Coulombic efficiency (CE) in zinc metal anodes by co-engineering salts and solvents to address two critical factors: plating morphology and the anode-electrolyte interface. By integrating a dual-salt approach and organic co-solvent design, these issues can be effectively addressed. The resulting hybrid dual-salt electrolyte renders CE of 99.95% at 1 mA cm⁻² at a medium concentration (3.5 m). Building upon the near-unity CE, an anode-free cell with ZnI₂ cathode can stably run more than 1000 cycles under practical conditions with minimal capacity loss. Our findings provide a promising pathway for the design of reversible metal anodes, advancing metal-based battery technologies for broader energy storage applications.

The increasing demand for grid energy storage in modern society continues to propel the global battery industry^{1–3}. The transition to TWh-scale energy storage presents new challenges in battery performance, especially battery cost, sustainability, and intrinsic safety^{4–6}. Lithium-ion batteries, with their high energy density (>150 Wh kg⁻¹), currently dominate the market of energy storage batteries. However, the low identified resources of lithium and the flammability and toxicity of the organic electrolytes pose a critical challenge to sustainability. Aqueous batteries, compared to commercial lithium-ion batteries, offer significant advantages in cost-effectiveness, recyclability and safety, positioning them as strong contenders in grid energy storage^{7,8}. And zinc metal has emerged as an ideal candidate for aqueous anodes due to its low redox potential, high theoretical capacity, and abundant availability, making aqueous zinc metal batteries (ZMBs) a promising alternative for grid energy storage^{9–11}. ZMBs require high reversibility to meet the extended operational demands

of grid energy storage. To illustrate, the CE for the plating and stripping of zinc must surpass 99.97% to facilitate 5000 cycles at 60% end-of-life for a ZMB with an N/P ratio of 2. However, challenges like corrosion¹² and dendrite formation¹³ hinder achieving high CE and long lifespan, significantly impeding ZMBs development.

Numerous efforts have been made to enhance the reversibility of the Zn anode, encompassing electrolyte engineering^{14–18}, crystal-facet manipulation^{19–23}, various coatings^{24–28}, and substrate optimization^{29–31}. These advancements have greatly improved the cycle life of the Zn anode. However, achieving a near-unity CE, especially at current densities of 1 mA cm⁻² and below, remains a significant challenge¹⁷. The difficulty in achieving near-unity CE arises from corrosion and HER issues in aqueous electrolytes, which are inherently tied to the low potential of Zn metal and controlled by thermodynamics. To make matters worse, dendrite formation can greatly exacerbate these side reactions. As a result, satisfactory CE (>99.9%) have remained elusive³².

¹School of Materials and Energy, University of Electronic Science and Technology of China, Chengdu, PR China. ²School of Physical and Mathematical Sciences, Nanyang Technological University, Singapore, Singapore. ³Hubei Key Laboratory of Micro-Nanoelectronic Materials and Devices, School of Microelectronics, Hubei University, Wuhan, PR China. ⁴College of Materials Science and Engineering, Sichuan University, Chengdu, PR China. ⁵Institute of Sustainability for Chemical, Energy and Environment (ISCE2), Agency for Science Technology and Research (A*STAR), Singapore, Singapore. ⁶Institute of Materials Research and Engineering (IMRE), Agency for Science, Technology and Research (A*STAR), Singapore, Singapore. ⁷Department of Chemistry, National University of Singapore, Singapore, Singapore. ⁸These authors contributed equally: Bao Zhang, Jia Yao. ✉e-mail: weisun@uestc.edu.cn; houzhaowan@hubu.edu.cn; fanhj@ntu.edu.sg

This CE challenge is the same for other metal anodes^{33,34}. Concentrated electrolytes have been proposed to extend the electrochemical stability window of aqueous electrolytes, enabling high CE of the Zn anode^{9,35,36}. However, these highly concentrated electrolytes face challenges such as low ionic conductivity and high viscosity, posing barriers to commercialization.

Given the distinctive plating/stripping chemistry of metal anodes, a singular approach is typically insufficient to achieving highly reversible metal chemistry. An integration of multiple approaches is necessary, yet their interaction must be carefully regulated to prevent adverse effects. Different from highly concentrated electrolytes, commercial lithium-ion batteries are built on a cocktail strategy of various solvents and additives, each contributing to the overall electrolyte performance. In this study, we explore electrolyte design principles and apply this cocktail strategy to Zn metal chemistry towards high CE at moderate concentrations. Our approach involves a dual-salt strategy for the purpose of promoting homogeneous Zn deposition through anion-rich Zn²⁺ solvation structures. The other aspect of our cocktail strategy is to identify by theoretical screening appropriate organic co-solvents to inhibit corrosion and hydrogen evolution through reduced water activity. These anion-rich solvation structures and organic co-solvents facilitate the formation of a solid electrolyte interphase (SEI). The resulting hybrid dual-salt electrolyte (HDE) renders high reversibility for Zn stripping/plating, with over 99.95% CE at 1 mA cm⁻² with a moderate concentration (3.5 m). Furthermore, this HDE imparts high cycling stability to Cu||Zn||₂ anode-

free batteries, maintaining more than 95% capacity after 1000 cycles under practical conditions.

Results

Design principles of cocktail strategy

The irreversibility of Zn plating/stripping process is mainly attributed to dead Zn (Q_{deadM}), corrosion (Q_{cor}) and hydrogen evolution reaction (HER, Q_{HER}). The irreversible aspect of Q_{HER} intricately is associated with the thermodynamic properties of electrolyte (specifically, water activity) and catalytic behavior of the anode-electrolyte interface. Q_{cor} shares a similar dependence on water activity and interfacial properties. Q_{deadM} , on the other hand, arises from Zn dendrites and is exacerbated by Q_{cor} and Q_{HER} , playing a major role in calendar aging^{37,38}. The irreversibility associated with Q_{cor} and Q_{HER} is also closely intertwined with the inhomogeneous deposition of Zn, highlighting that these irreversible components are interconnected. Hence, achieving a high CE of the Zn anode necessitates both homogeneous Zn deposition and a relatively ‘inert’ anode-electrolyte interface. This inert interface may exhibit suppressed kinetics, such as the formation of a passivated interphase, or hindered thermodynamics, such as the reduction of water activity.

In response to the above irreversible aspects, we can take two key steps (Fig. 1a): (1) fine-tuning the Zn²⁺ solvation structures to achieve uniform zinc deposition, (2) customizing the inner Helmholtz plane to reduce water activity. Furthermore, the formation of a robust SEI is highly related to how we design the solvation structures and co-

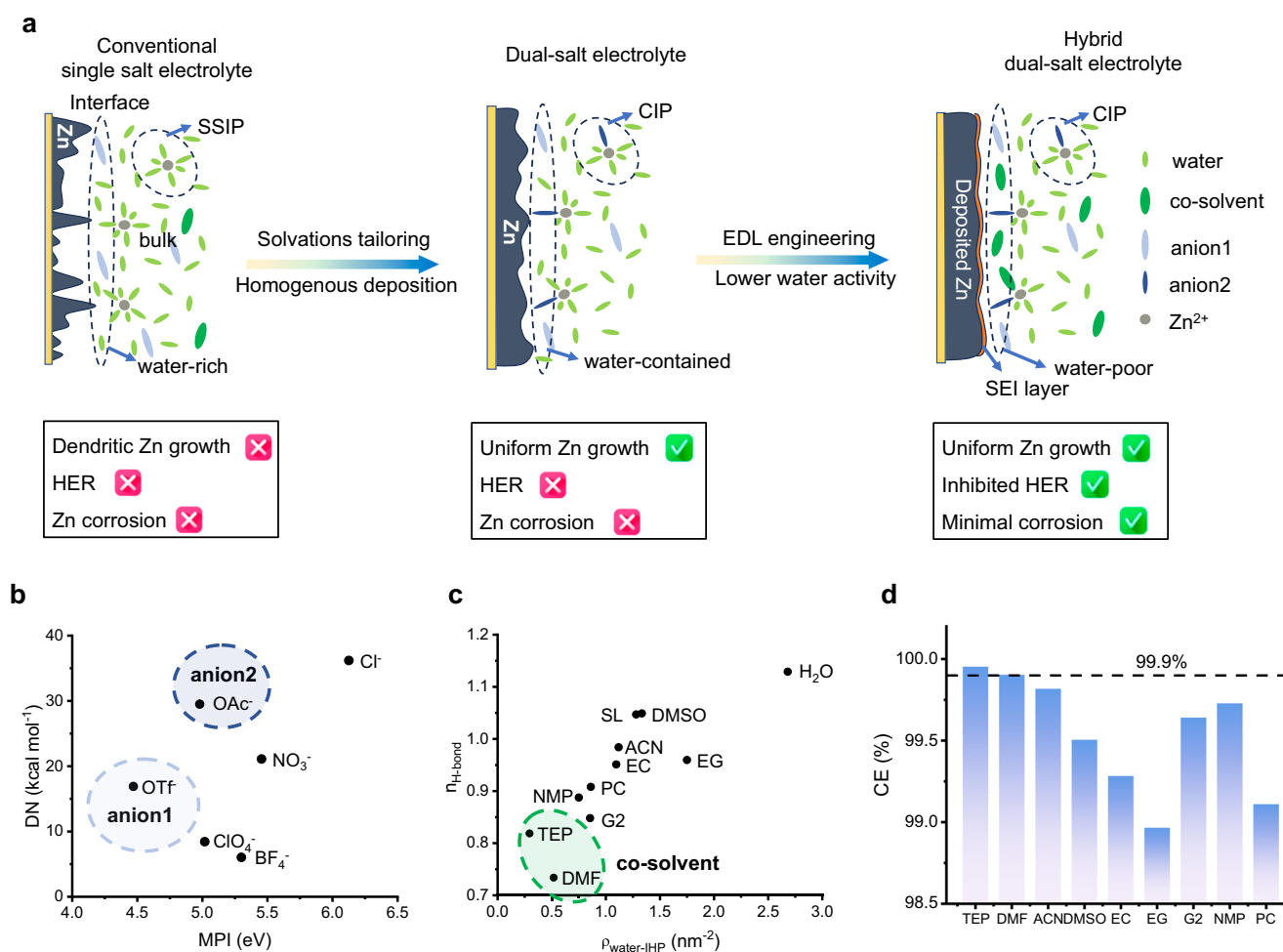


Fig. 1 | Design principle and the realization of cocktail strategy for Zn metal anode. a Illustration of cocktail strategy and hybrid dual-salt electrolyte design. **b, c** Rational selection of dual-salts and co-solvent. **d** The average CEs of various hybrid dual-salt electrolytes based on 10th–100th cycles.

solvents. Concerning Zn^{2+} solvation structures, contact-ion pairs (CIP) solvation structures were found conducive to promote more homogeneous metal deposition by reducing the exchange current density in alkali metal batteries³⁹. High donor number anion depicts a strong affinity between the cation and anion and are more likely to form CIP solvation structures. As shown in Fig. 1b, acetate (OAc^-) shows much higher donor number among common non-corrosive anions. As discussed in the Figs. S1–S3, OAc^- is more likely to form CIP structures than the widely used sulfate and triflate (OTf^-) ions, promoting uniform Zn deposition. But the former has the drawback of lower solubility. In contrast, the low-polarity triflate possesses higher solubility and a more hydrophobic double-layer structure⁴⁰, diminishing corrosion and HER. This inspires us to explore a dual-salt approach.

To construct an ‘inert’ anode-electrolyte interface, a co-solvent approach is deployed. We first screened some common organic co-solvents by theoretical calculations. The free-water density and H-bond number of water in inner Helmholtz plane are calculated using classic molecular dynamics simulations (Fig. S4). Triethyl phosphate (TEP) and dimethylformamide (DMF) are selected as rational co-solvent because they can induce the free-water-poor inner Helmholtz plane (within 5 Å from the electrode) and reduce the interfacial water activity (Fig. 1c). And it has been shown that both CIP structures and organic co-solvent will support the SEI formation^{41,42}. Therefore, a cocktail strategy combining a dual-salt and organic co-solvent approach is expected to promote uniform Zn deposition while

inhibiting corrosion and HER, as confirmed in Fig. 1d. It should be noted that approaches of individual components, such as co-solvent engineering using DMF^{43–45} or TEP^{46–49}, have been extensively applied in the design of ZMBs electrolytes. However, these approaches have typically resulted in CE below 99.8%, even when incorporating a high content of organic co-solvents (Supplementary Table 1). The unique plating/stripping chemistry of metal anodes makes their requirements for the electrolyte more stringent. Likewise, the concept of the cocktail strategy maintains its consistency across both aqueous and nonaqueous systems, with the goal of achieving enhanced comprehensive performance through the integration of multiple effects. The key difference lies in the management of these effects: in aqueous systems, the regulation of water activity is paramount, whereas in nonaqueous systems, the formation and control of the SEI take precedence.

Reversibility of Zn metal anode

Commencing with a plating/stripping test at 1 mA cm^{-2} and 1 mAh cm^{-2} , we compare the CEs of three types of electrolytes, viz., 4 m ZnOTf_2 (single salt electrolyte, SE), 4 m $\text{ZnOTf}_2 + 1 \text{ m ZnOAc}_2$ (dual-salt electrolyte, DE), and 2.8 m $\text{ZnOTf}_2 + 0.7 \text{ m ZnOAc}_2 + 30 \text{ wt\% DMF}$ (hybrid dual-salt electrolyte, HDE). The concentrations of dual-salt and co-solvent were optimized through CE values (Fig. S5). The SE exhibits an average CE of 99.3% and short-circuit after less than 100 cycles (Fig. 2a). Issues related to side reactions and dead zinc has contributed to the low reversibility and CE (Figs. S6, S7), as well as poor calendar

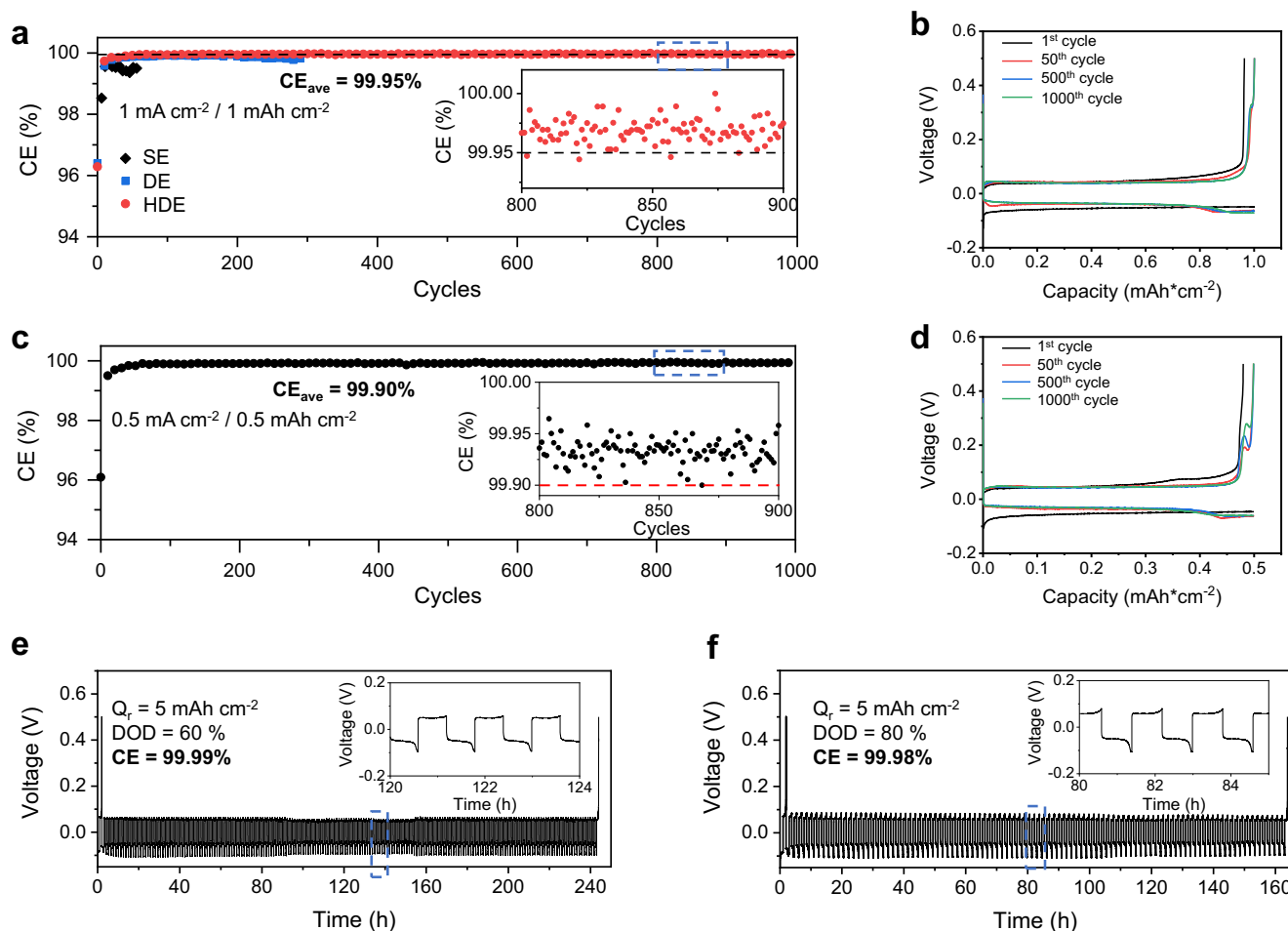


Fig. 2 | Coulombic efficiencies of different electrolytes. Zn plating/stripping CE with magnified views of selected cycles between 800th cycle to 9000th cycle in at (a) 1.0 mA cm^{-2} and 1.0 mAh cm^{-2} and (c) 0.5 mA cm^{-2} and 0.5 mAh cm^{-2} . Zn plating/stripping potential profiles on a Cu electrode cycled in HDE at (b) 1.0 mA cm^{-2} and

1.0 mAh cm^{-2} and (d) 0.5 mA cm^{-2} and 0.5 mAh cm^{-2} . e, f CE tests under ‘reservoir half-cell’ galvanostatic protocol. A fixed capacity of Zn (5 mA cm^{-2} , 5 mAh cm^{-2}) is firstly plated, followed by plating/stripping at a fixed DOD of 60% (200 cycles) and 80% (100 cycles).

aging property (Fig. S8). Similarly, the Zn||Zn symmetric cell with SE encounters quick short-circuit, primarily due to uneven Zn deposition (Fig. S9). Upon the introduction of the dual-salt electrolyte, the CE significantly improves, reaching an average of 99.8%. With further inclusion of co-solvents, DMF and TEP exhibit the highest CE among these tested co-solvents, proving the validity of theoretical screening (Fig. S10). The average CEs of HDE reaches 99.95% (based on an average of 1000 cycles) and stabilizes at approximately 99.97%. The other four individual cells utilizing HDE also exhibit similar average CEs, around 99.95% (Fig. S11). On the contrary, both the single salt electrolyte with ZnOAc₂ and hybrid electrolyte with single salt of ZnOTf₂ exhibit unsatisfactory CEs of <99.5% (Fig. S10). This achievement of HDE represents one of the highest reported CEs in the literature (Supplementary Table 1). Furthermore, both DE and HDE can enable stable cycling of Zn||Zn symmetric cell for more than 2000 h (Fig. S9). HDE also facilitates stable cycling of zinc foils at a high depth of discharge (DOD) of 60% for over 600 h (Fig. S12).

In general, low current densities will amplify the effects of HER and corrosion. In our test at a current density of 0.5 mA cm⁻², HDE still achieves average CEs of 99.90% and a stabilized CE of 99.93%. Furthermore, achieving high CEs at high areal capacities presents another challenge for practical applications. As shown in Fig. S13, our HDE can attain a CE of 99.9% within the initial 5 cycles and sustain this level of efficiency even at an areal capacity of 5 mAh cm⁻² under a current density of 1 mA cm⁻². Aurbach's galvanostatic protocol was additionally employed to evaluate CE at high DOD. The CE approaches almost 100% at high DODs of 60% and 80%. In contrast, SE fails the test and DE shows a CE of only 99.7% (Fig. S14). Moreover, HDE offers notably low temperature ionic conductivity (3.2 mS cm⁻¹ at -40 °C) and a wider electrochemical window (Fig. S15). HDE also shows a higher zinc ion transference number of 0.41, but it was still not sufficient (Fig. S16). It should be noted that this strategy is not applicable for harsh condition of very high current density and very high areal capacity (Fig. S13d). Fast deposition of zinc metal may no longer be dominated by CIP solvation structures, but rather by SSIP solvation structures with faster kinetics, thus leading to short circuits.

To demonstrate the adaptability of our cocktail strategy, we substituted the highly soluble triflate with high-concentrate ZnCl₂ and obtained CEs exceeding 99.9% (Fig. S17). Moreover, we explored the substitution of the ZnOTf₂ separately with the hydrophobic ZnTFSI₂ and substitution with hydrophobic quaternary ammonium salts. The obtained CEs from these two electrolytes at 1 mA cm⁻², 1 mAh cm⁻² with a medium concentration exceed 99.9% (Fig. S18), validating the universality of our cocktail strategy.

Characterization of solvation structure and hydration structure

To investigate the origin of the high CEs in HDE, we conducted comprehensive characterization to understand the solvation structures and water environments in these electrolytes. Fourier transform infrared spectroscopy (FTIR) can reveal the evolution of water environments. As illustrated in Fig. 3a, the intensity of O-H stretching (3200–3600 cm⁻¹) of H₂O in SE at higher wavenumbers range decreases with the introduction of OAc⁻ (Supplementary Table 2). Specifically, three hydrogen-bond states were identified in the water structure^{36,50}: strong H-bond (3263.8 cm⁻¹), weak H-bond (3247.3 cm⁻¹), and none H-bond (3549.2 cm⁻¹). The decrease in strong H-bond content in DE and HDE is related to the zinc ion concentration and the presence of the DMF co-solvent. The solvation sheath of zinc ions as well as DMF co-solvent disrupt the hydrogen-bonding network between water molecules, thereby reducing water reactivity. Furthermore, gas chromatography tests (Fig. S19) demonstrated that DE and HDE has effectively inhibited HER.

Raman spectroscopy was employed to reveal the solvation structures of Zn²⁺ (Fig. 3b–d). The -SO₃ stretching modes (1000–1080 cm⁻¹) of OTf⁻ were utilized to identify OTf⁻ involved

solvation structures⁴². Limited reports are available regarding the OAc⁻ involved solvation structure identification. A blue shift of ν_s(C=O) is observed with an increased content of OAc⁻ (Fig. S20), indicating that solvated OAc⁻ may introduce a blueshift in ν_s(C=O), similar to the trend of the -SO₃ stretching modes of OTf⁻. This means that ν_s(C=O) can be used to identify OAc⁻ involved solvation structures. Moreover, the Raman peaks were deconvoluted into solvent-separated ion pair (SSIP), contact ion pair (CIP), and aggregate (AGG). In SE, the proportion of CIP (1042.3 cm⁻¹) is approximately 36.9% (Supplementary Table 3), suggesting that the dominant solvation structure contains (Zn-(H₂O)₆)²⁺. Intriguingly, the coordination number of OTf⁻ is slightly reduced after the introduction of acetate, with acetate entering in the coordination of Zn²⁺ in DE (64.5%, 1448.3 cm⁻¹). This indicates that acetate is more competitive for Zn²⁺ solvation structures in the dual-salt⁴², replacing part of the OTf⁻ solvation, in line with the solvation energy trend (Fig. S21), *viz.*, (Zn-OAc-(H₂O)₅)⁺ (20.5 eV) > ((Zn-OTf-(H₂O)₅)⁺ (19.8 eV). The introduction of a significant amount of acetate in the sheath also led to the appearance of AGG (12.4%, 1473.1 cm⁻¹) in DE. In HDE, the introduction of DMF increased the coordination number of OTf⁻. The case of OAc⁻ becomes more complicated and it is difficult to obtain the exact proportions in HDE. Nonetheless, the proportion of OAc⁻ is significantly decreased compared to DE (Fig. S20). The decrease in AGG is favorable for the increase in electrolyte ionic conductance, especially at low temperatures.

The solvation structures were further studied by X-ray absorption near-edge structure (XANES) and extended X-ray absorption fine structure (EXAFS) analysis of Zn K-edge (Fig. 3e, f). Compared with 1 M ZnOAc₂ electrolyte, the 4 M ZnOTf₂ exhibits lower edge energy in the XANES spectrum (Fig. 3e). This difference may be attributed to variations in the electron-donating ability between OTf⁻ and OAc⁻. And the ESP analysis indicates the charge of Zn²⁺ in OTf⁻ involved CIP (+1.116) is lower than that in OAc⁻ involved CIP (+1.270). In the DE, the presence of more CIP structures leads to a shift of the K-edge energy to lower values. The introduction of DMF induces further alterations in the solvation structure. As a result, the K-edge shift to higher energies due to a reduction in the CIP content and the entry of DMF into the sheath. EXAFS spectra in R space confirm the rearrangement of the local solvation structure upon the introduction of DMF (Fig. 3f).

Molecular dynamics (MD) simulations were performed to provide additional insights into the structure of these electrolytes (Figs. 3g, S22–S25). The evolution of water environments influences the order of the H-bond network, resulting in less ice-like water. The tetrahedral order parameter of water moves towards a more disordered state, impacting the low-temperature ionic conductance of the electrolyte. Consequently, HDE exhibits superior low-temperature ionic conductance. The solvation structures are also confirmed in the simulations. In SE, SSIP is the primary component. The SSIP content decreases to 50.4% in DE, with OAc⁻ entering the solvation sheath from a larger proportion. A high proportion of AGG in DE adversely affects ionic conductance (Fig. S17). In HDE, SSIP content is further reduced, and the proportion of AGG in DE also decreases. The simulations also confirm that DMF enters the solvation sheath of Zn²⁺ with a coordination number of 0.19 (Fig. S24). All these results imply that the dual-salt introduces more anions into the Zn²⁺ primary solvation sheath, and the DMF co-solvent is also able to enter the solvation sheath.

Zn plating/stripping morphology and SEI chemistry

We assessed the morphology of plated Zn and Zn after soaking in different electrolytes. The current density reports an important role in deposition morphology. In DE and HDE, high current density leads to more uneven deposition morphology. Nevertheless, the elevated CIP content in DE and HDE leads to more uniform Zn nucleation and smoother deposition under plating currents of 1 and 5 mA cm⁻² (Figs. S26, S27). Moreover, the HDE results Zn surface with more exposed (002)Zn planes, which also contributes to the higher stability

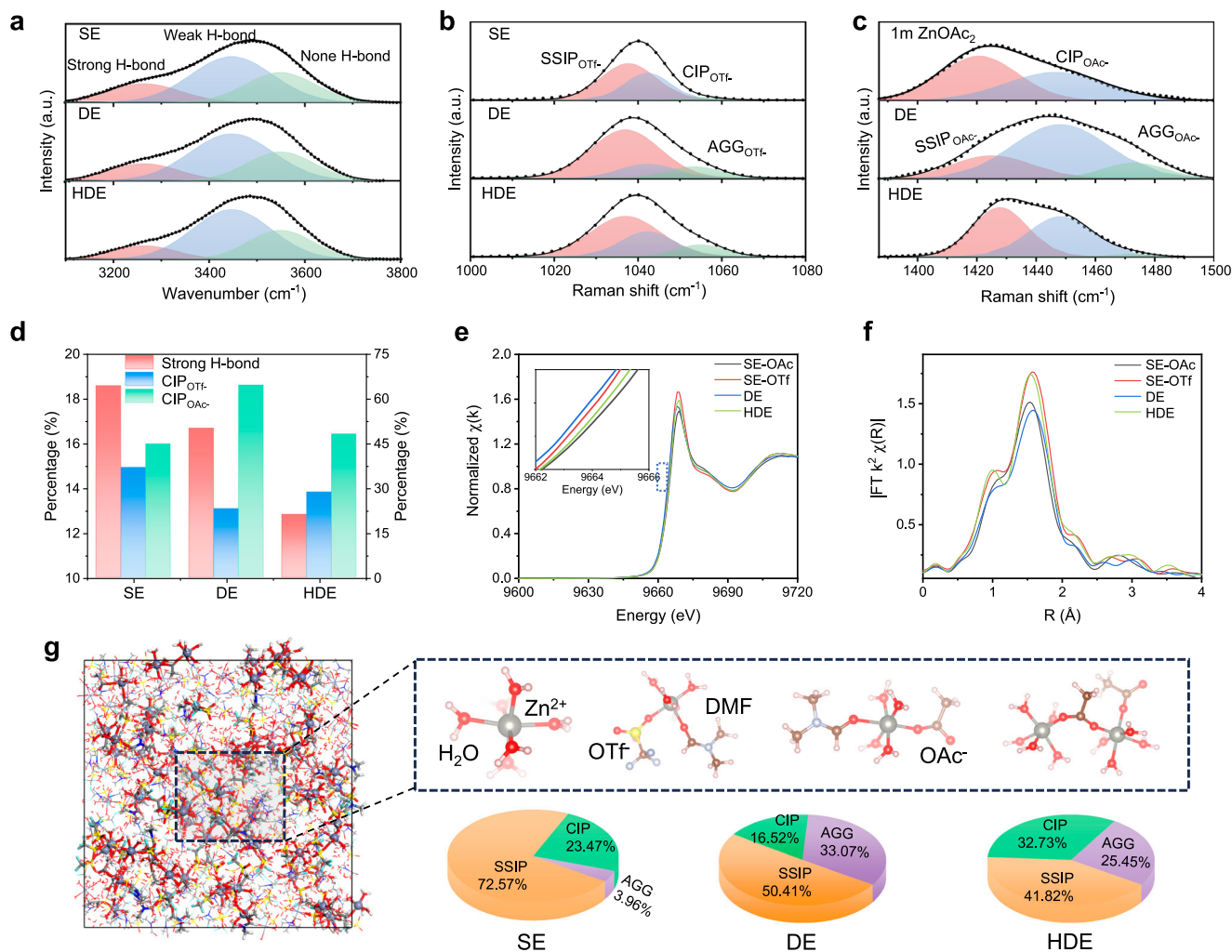


Fig. 3 | Characterization of solvation structures and H₂O structure. **a** FTIR spectra of various electrolytes at the wavenumber range of O-H stretching vibration. **b, c** Raman spectra in the wavenumber region of the SO₃ stretching modes and symmetric C=O stretching modes, respectively. **d** Strong H-bond contents and CIP

solvation structures contents of various electrolytes. **e** The XANES spectra and **(f)** EXAFS spectra in *R* space of various electrolytes. **g** MD simulation snapshot and typical solvation structures of HDE, and distribution percentage of possible main solvation sheath components of various electrolytes.

of Zn metal anode (Fig. S28). This uniform Zn nucleation and deposition was further verified by chronoamperometry (CA) (Fig. S29). The variation of current at constant overpotential correlates with the nucleation process. In SE, the current continuously increases within 600 s, which represents an uneven nucleation process and rough three-dimensional propagation. HDE and DE, on the other hand, both exhibit two-dimensional like growth mode.

Immersion tests demonstrate that, compared to SE and DE, corrosion is significantly reduced in HDE (Figs. S30–S32). Dendrite formation and corrosion byproduct are obvious in SE, but much less on DE and nearly absent in HDE (Figs. 4a, S33, S34), highlighting the superior anti-corrosion property rendered by HDE. The water-deficient inner Helmholtz plane contributes to the corrosion-resistant interface (Figs. S35, S36). In the in-situ optical microscopy observation, the plated Zn becomes rough with dendrite formation after 20 minutes of plating with clear gas bubble formation in SE (Fig. 4d). Conversely, both DE and HDE electrolytes enable flat and compact Zn plating (Figs. 4e, S37). Surface 3D reconstructions of plated Zn also confirm the much more homogeneous Zn deposition with DE and HDE (Fig. 4c).

CIP structures in aqueous batteries, particularly those containing fluorine-containing anions, have been reported to promote dense SEI formation. This is consistent with organic co-solvents. We examined

the surface structure of cycled Zn in HDE using X-ray photoelectron spectroscopy (XPS), time-of-flight secondary ion mass spectrometry (ToF-SIMS), and transmission electron microscopy (TEM). XPS tests show a predominance of oxides in the SEI (Figs. S38, S39), which is consistent with the results of the soaking tests. As shown in Fig. 5a, the peaks at approximately 688.6 eV and ~684 eV in the F 1s spectrum are attributed to *CF₃ and ZnF₂, respectively. After Ar⁺ sputtering for 100 s, the F 1s peak is predominated by ZnF₂, indicating the presence of a ZnF₂-contained SEI structure. Theoretical calculations (Fig. S40) and XPS tests (Fig. S41) reveal that ZnF₂ is derived from solvated OTf ion. The C 1s profiles in Fig. 5b indicate the presence of some ZnCO₃ (~289.1 eV) on the top surface of Zn, which can be attributed to the decomposition of acetate ions and DMF (Fig. S42). ToF-SIMS results further confirm the presence of ZnF₂ in the SEI, while ZnCO₃ is found in only small amounts at the top surface (Fig. 5c). TEM tests reveal that the SEI thickness ranges from approximately 50 to 100 nm and is rich in inorganic components (Fig. S43). This robust SEI plays a crucial role in passivating the Zn anode and suppressing side reactions (Fig. 5d).

Full-cell performance

We further examined the reversibility of full cells in HDE, including Zn || ZnI₂ cell, Zn || vanadium oxide full cell, and Zn || activated carbon (AC) cell. As illustrated in Fig. 6a, the SE supports only around 200

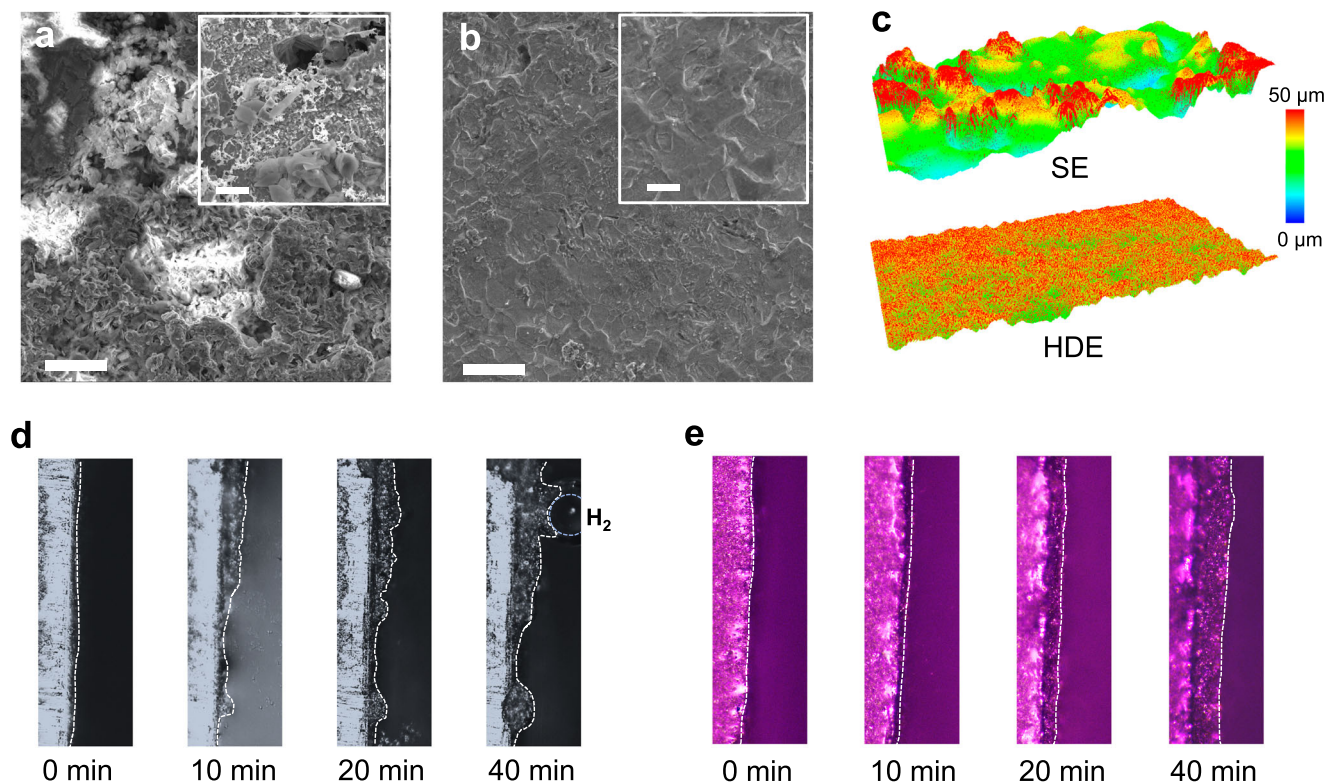


Fig. 4 | The morphology of plated Zn. SEM images of Zn anode after 50 cycles at 1 mA cm^{-2} and 1 mAh cm^{-2} in (a) SE and (b) HDE. Scale bar: $30 \mu\text{m}$ in a and $2 \mu\text{m}$ in (b) (magnified view). c 3D height images of plated Zn in SE and HDE with a capacity of

5 mAh cm^{-2} at 5 mA cm^{-2} . In-situ optical microscopy images of Zn plating in (d) SE and (e) HDE at a current density of 5 mA cm^{-2} .

cycles of Zn || ZnI₂ cell at a NP ratio of ~ 0.8 . In contrast, HDE can prolong it to more than 3000 cycles without evident capacity degradation, maintaining approximately 97% of its initial capacity ($\sim 142.7 \text{ mAh mg}^{-1}$). Such near-unity CE of HDE can enable anode-free Cu || ZnI₂ batteries to cycle more than 1000 times with minimal capacity loss, preserving more than 95% of its initial capacity. Additionally, the anode-free Cu || ZnI₂ cell under practical conditions, high areal mass loading ($>20 \text{ mg cm}^{-2}$) and lean electrolyte ($\sim 10 \mu\text{L mAh}^{-1}$), retains over 80% of its initial capacity after 300 cycles at 0.15 A g^{-1} (Fig. 6c). Zn || ZnI₂ cell with NP ratio about 1.0 demonstrate a similar decay rate with this anode-free cell (Fig. S44), suggesting the iodine dominates the cell capacity degradation. When a CCCV charge protocol ($1.6 \text{ V} / 50 \text{ mA g}^{-1}$) was employed, the anode-free Cu || ZnI₂ cell can be stably cycled at a high mass loading for more than 1000 cycles without significant capacity degradation. This anode-free Cu || ZnI₂ cell exhibits good rate performance and low self-discharge characteristics (Figs. S45, S46). The specific energy density of this anode-free cell reaches 82 Wh kg^{-1} based on the total mass of electrodes. Further introduction of Br or Cl increases the energy density to 113 and 145 Wh kg^{-1} , respectively (Fig. S47).

High mass loading vanadium oxide cell also demonstrates stable cycling for 300 cycles under practical conditions (Figs. 6d, S48). In addition, due to the high ionic conductivity and non-flammable nature of HDE (Fig. S49), the Zn || V₂O₅ cell remains stable cycling from -40°C to 50°C (Figs. S50–S52). We also validated the stable cycling performance of large anode-free Cu || ZnI₂ pouch cells (Fig. S53).

Discussion

We have demonstrated a cocktail strategy to design hybrid electrolytes for zinc metal batteries. Integrating a high donor number acetate salt and a highly soluble triflate salt results in a dual-salt electrolyte with a solvation structure rich in CIP and a hydrophobic

IHP structure. The dual-salt configuration promotes uniform zinc deposition while suppressing corrosion and hydrogen evolution side reactions. The simultaneous addition of organic co-solvents, such as DMF or TEP, further reduces water activity and facilitates the formation of a robust SEI. As a result, this HDE renders highly reversible Zn plating and stripping, achieving a high CE of 99.95% at a current density of 1 mA cm^{-2} . We have conducted extensive characterizations to delve into the fundamental properties of this hybrid dual-salt system. As proof-of-concept demonstration, we have implemented such hybrid system in an anode-free Cu || ZnI₂ full cell, which shows long-cycle stability under practical conditions.

The cocktail strategy presented here offers a rational and promising approach to achieving highly reversible aqueous metal batteries chemistry. For the case of MnO₂ cathode (Fig. S54) which is chemically unstable, one may consider introducing additional effects into the cocktail strategy to achieve highly stable ZMBs with high specific energy density. Finally, similar to zinc, most metal-based batteries, such as aqueous manganese- and aluminum-metal batteries, also face challenges related to dendrite formation and side reactions, which will deteriorate battery performance and safety. By leveraging the distinct features of different salts and solvents, this cocktail strategy may guide the design of hybrid electrolyte systems to address these challenges.

Methods

Chemicals

Zinc triflate (ZnOTf₂, $>99\%$), Zn sulfate (ZnSO₄·7H₂O, AR), anhydrous zinc chloride (ZnCl₂, $>99\%$) and Zn acetate (ZnOAc₂, AR) were purchased from Adamas, Sinopharm, Sigma-Aldrich and Macklin, respectively. Dimethylformamide (DMF, $>99.8\%$) and triethyl phosphate (TEP, $>98\%$) were purchased from BLDpharm and Sigma-Aldrich,

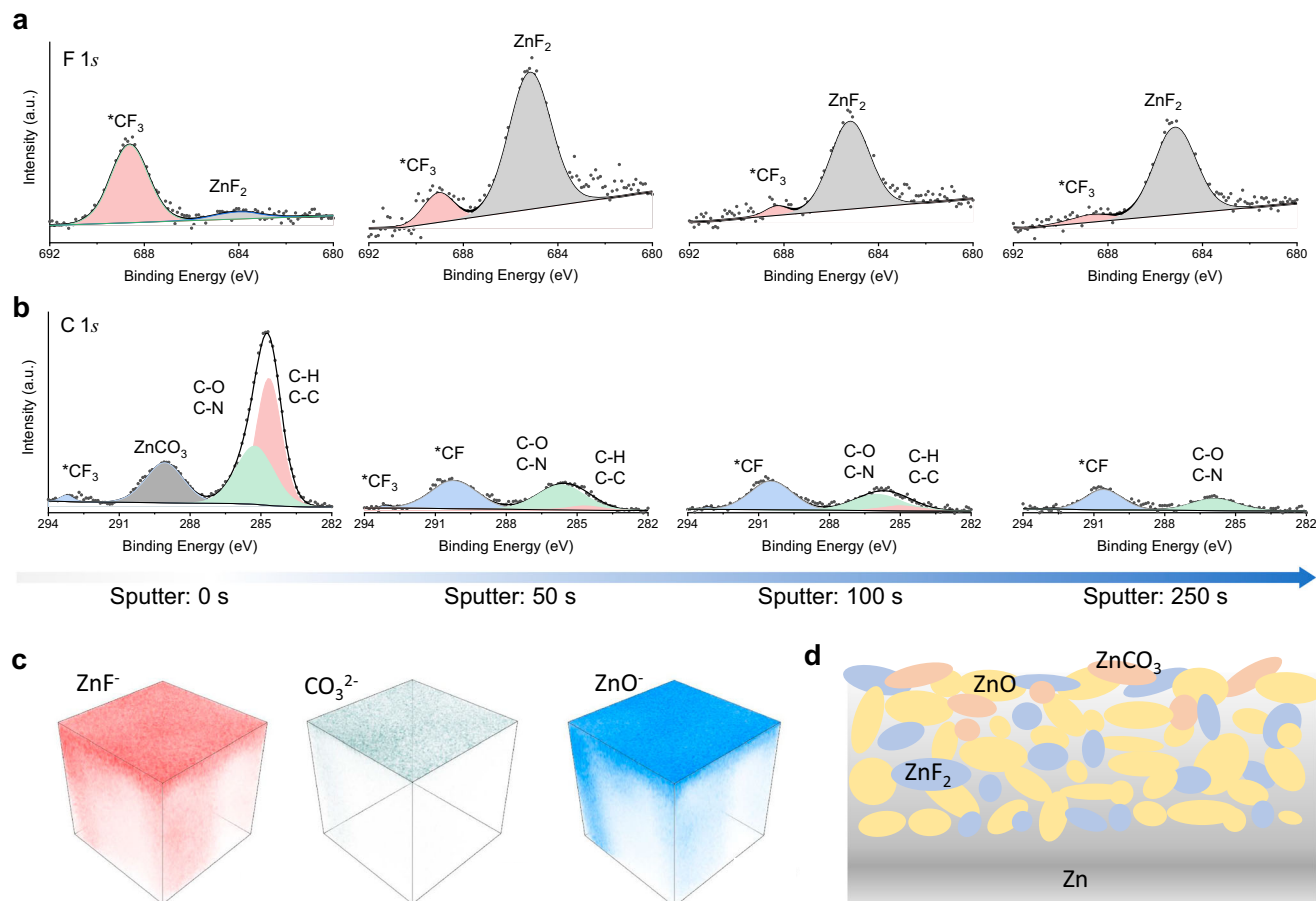


Fig. 5 | Characterizations of SEI on cycled Zn. Depth-resolved XPS of (a) C 1s spectra, and (b) FIs after 50 cycles in HDE. c TOF-SIMS color mappings of ZnF^- , CO_3^{2-} , and ZnO^- fragments. Test area is $50\ \mu\text{m} \times 50\ \mu\text{m}$. d Schematic presentation of proposed inorganic rich SEI.

respectively. Zn metal foils were purchased from Hebei Qingyuan Metal Material Technology Co., Ltd.

Preparation of electrolytes and electrodes

All the aqueous electrolytes were prepared by dissolving Zn salts into DI water. The hybrid electrolytes were prepared by dissolving various mass ratios (to the weight of water) of organic solvent in the aqueous electrolytes. Vanadium oxide nanobelt was synthesized based on previous report¹. Typically, 3 g V_2O_5 (>98%, Sigma-Aldrich) powder was added into 100 mL 2 mol/L NaCl solution and stirred for 48 h at room temperature. The brown powder was filtered, washed and dried overnight at 60°C . For ZnI_2 cathodes preparation with medium mass loading, first, a mixture of activated carbon, super P conductive carbon and PVDF binder (weight ratio of 8:1:1) was coated on a carbon paper with a mass loading of $\sim 12\ \text{mg cm}^{-2}$. Then, an ethanol solution of ZnI_2 (0.1 M) was drop coated on the activated carbon electrode and vacuum dried at 120°C . For $\text{Zn}||\text{ZnI}_2$ coin cells, Cu foils pre-electrodeposited with Zn was used as anode, and 100 μL of electrolyte was added. For ZnI_2 cathodes with high mass loading, a mixture of active material ZnI_2 , activated carbon, CNTs and PTFE binder was pressed to form free-standing electrodes in a weight ratio of 6:6:1:1. The operating voltage range for ZnI_2 -based full batteries was 0.6–1.6 V under room temperature conditions ($\sim 20^\circ\text{C}$). Pouch cell shared the same method. For V_2O_5 cathodes preparation, a mixture of active material V_2O_5 , CNTs and PTFE binder was pressed on a carbon paper in a weight ratio of 7:2:1.

Cell assembling

The $\text{Zn}||\text{Cu}$ cells were assembled with Zn foil, Cu foil, and glass fiber separator. Zn symmetric cells were fabricated using Zn foils and a glass

fiber separator. If not specified otherwise, Zn foils with a thickness of $100\ \mu\text{m}$ and a diameter of 12 mm were used in half-cell configurations. The electrolyte volume for each cell was maintained at $60\ \mu\text{L}$. The NP ratio of full cell is defined as the ratio of the capacity of the anode to the cathode. For the anode-free $\text{Cu}||\text{ZnI}_2$ cell, the NP ratio is 0. For the $\text{Zn}||\text{ZnI}_2$ cells in Fig. 6a, we first plated 1 mAh of zinc on the surface of the copper foil as the anode, so the NP ratio is close to 0.8. For $\text{Zn}||\text{V}_2\text{O}_5$ cells, a $10\ \mu\text{m}$ zinc foil is employed as anode with theoretical areal capacity of about $5.8\ \text{mAh cm}^{-2}$, so the NP ratio is about to 1.7. The half cells were tested in an open environment, while the full cells were evaluated in an environmental chamber. Unless otherwise specified, both half cells and full cells were tested at approximately 20°C using regular coin cells (2032 type, made of 316 stainless steel). The diameters of the cathodes, anodes, and separators were 12 mm, 12 mm, and 14 mm, respectively. The specific energy density was calculated using the formula: $E_{sp} = \frac{E_{dsg}}{m_a + m_c}$. Here E_{dsg} is the discharge energy, and m_a and m_c are the total mass of the anode and cathode electrodes, respectively.

Electrochemical tests

Ionic conductivity measurements were performed using custom-made cells equipped with two platinum electrodes and calibrated using a standard conductivity solution (Mettler Toledo, $12.88\ \text{mS cm}^{-1}$). Aurbach's protocol was utilized for CE tests at high depth of discharge (DOD). Initially, a fixed capacity of Zn ($5\ \text{mAh cm}^{-2}$, denoted as Q_i) was plated and stripped on a Cu foil at a current density of $5\ \text{mA cm}^{-2}$. Subsequently, the same capacity of Zn was plated as a reservoir, followed by plating and stripping at a fixed capacity (Q_c). After several cycles (n), the final stripping process was carried out to a predefined

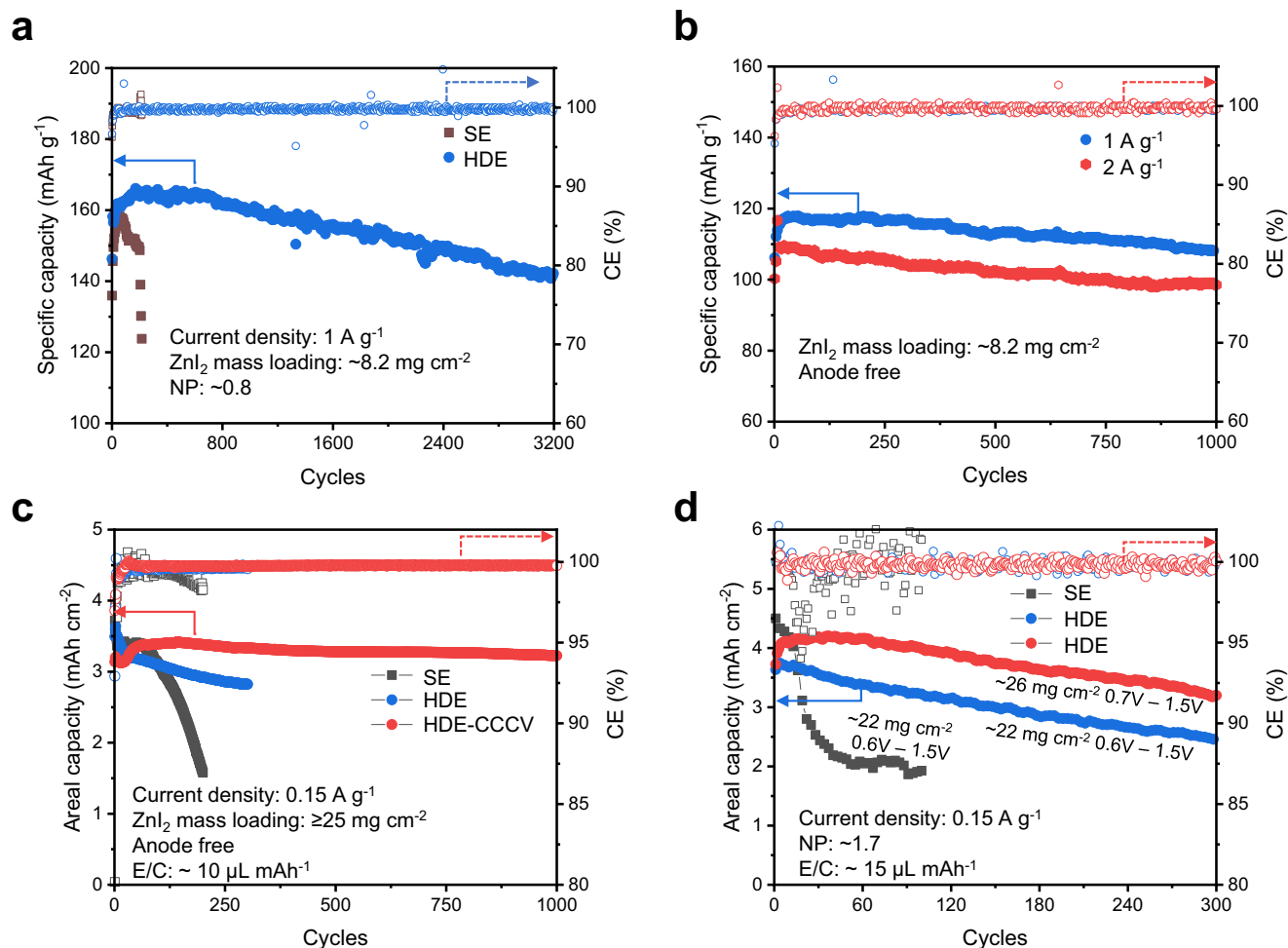


Fig. 6 | Electrochemical performance of full cells. a Anode-less cell cycling with a ZnI₂ cathode (mass loading of 8.2 mg cm⁻²) at 1 A g⁻¹. **b** Cycling performance of anode-free Cu | ZnI₂ cell. **c, d** Anode-free Cu | ZnI₂ cells and Zn | V₂O₅ cells cycling

performance under practical conditions (low current density and high mass loading of active materials). The ZnI₂ content in the CCCV test is 50 wt% and the rests are 43.2 wt%.

upper cut-off potential (0.5 V), corresponding to the remaining Zn (Q_s). The average CE was calculated using: $CE = \frac{n^+Q_c + Q_s}{n^+Q_c + Q_s}$. The electrochemical performance of the cells was evaluated using the Neware (Shenzhen) battery testing system (CT4008) at room temperature. Chronoamperometry (CA) and Tafel tests were conducted on a CHI760E electrochemical workstation. EIS tests were conducted on a Gamry 1010E electrochemical workstation.

Characterizations

Raman spectroscopy was conducted using a Horiba HR Evolution microscope with an excitation wavelength of 532 nm. FT-IR spectroscopy was performed with an attenuated total reflection (ATR) accessory on an instrument from Thermo Fisher Scientific, Frontier. X-ray adsorption fine structure (XAFS) analysis was carried out in transmission mode at the Singapore Synchrotron Light Source, specifically at the XAFCA beamline, and at the 8-BM beamline of the National Synchrotron Light Source II. XPS analysis was performed using a Thermo Fisher Scientific Model K-Alpha spectrometer equipped with Al Kα radiation (1486.6 eV). All XPS spectra were calibrated with the binding energy in the C 1s spectra set at 284.8 eV. High-resolution transmission electron microscopy (HRTEM) was conducted with a Talos F200X microscope (accelerating voltage 200.0 kV) to examine the solid-electrolyte interphase (SEI). XRD patterns were obtained using an advanced X-ray diffraction with Cu-Kα radiation (λ = 1.5418 nm). SEM images were acquired from a field emission

scanning electron microscope (JSM-7100 F). Ion distribution analysis was performed with time-of-flight secondary ion mass spectrometry (IONTOF GmbH, Germany measurements).

Data availability

Source data are provided with this paper. Configurations related to theoretical calculations and simulations are uploaded in MaterialsCloud (<https://doi.org/10.24435/materialscloud:qz-e6>). Source data are provided with this paper.

References

- Dunn, B., Kamath, H. & Tarascon, J.-M. Electrical energy storage for the grid: a battery of choices. *Science* **334**, 928–935 (2011).
- Zhu, Z. et al. Rechargeable batteries for grid scale energy storage. *Chem. Rev.* **122**, 16610–16751 (2022).
- Farivar, G. G. et al. Grid-connected energy storage systems: state-of-the-art and emerging technologies. *Proc. IEEE* **111**, 397–420 (2023).
- Liu, J. et al. The TWh challenge: next generation batteries for energy storage and electric vehicles. *Energy* **1**, 100015 (2023).
- Bussar, C. et al. Large-scale integration of renewable energies and impact on storage demand in a European renewable power system of 2050—sensitivity study. *J. Energy Storage* **6**, 1–10 (2016).
- Kurland, S. D. Energy use for GWh-scale lithium-ion battery production. *Environ. Res. Commun.* **2**, 012001 (2019).

7. Posada, J. O. G. et al. Aqueous batteries as grid scale energy storage solutions. *Renew. Sustain. Energy Rev.* **68**, 1174–1182 (2017).
8. Liang, Y. & Yao, Y. Designing modern aqueous batteries. *Nat. Rev. Mater.* **8**, 109–122 (2023).
9. Wang, F. et al. Highly reversible zinc metal anode for aqueous batteries. *Nat. Mater.* **17**, 543–549 (2018).
10. Khor, A. et al. Review of zinc-based hybrid flow batteries: from fundamentals to applications. *Mater. Today Energy* **8**, 80–108 (2018).
11. Cao, L. et al. Fluorinated interphase enables reversible aqueous zinc battery chemistries. *Nat. Nanotechnol.* **16**, 902–910 (2021).
12. Cai, Z., Wang, J. & Sun, Y. Anode corrosion in aqueous Zn metal batteries. *eScience* **3**, 100093 (2023).
13. Zuo, Y. et al. Zinc dendrite growth and inhibition strategies. *Mater. Today Energy* **20**, 100692 (2021).
14. Yang, F. et al. Understanding H₂ evolution electrochemistry to minimize solvated water impact on zinc-anode performance. *Adv. Mater.* **34**, 2206754 (2022).
15. Wang, Y. et al. Lean-water hydrogel electrolyte for zinc ion batteries. *Nat. Commun.* **14**, 3890 (2023).
16. Zhang, W. et al. Highly reversible zinc metal anode in a dilute aqueous electrolyte enabled by a pH buffer additive. *Angew. Chem. Int. Ed.* **62**, e202212695 (2023).
17. Jiang, H. et al. Chloride electrolyte enabled practical zinc metal battery with a near-unity Coulombic efficiency. *Nat. Sustain.* **6**, 806–815 (2023).
18. Wang, R. et al. Synergetic modulation on ionic association and solvation structure by electron-withdrawing effect for aqueous zinc-ion batteries. *Proc. Natl Acad. Sci.* **120**, e2221980120 (2023).
19. Zheng, J. et al. Reversible epitaxial electrodeposition of metals in battery anodes. *Science* **366**, 645–648 (2019).
20. Wang, J. et al. Stable interphase chemistry of textured Zn anode for rechargeable aqueous batteries. *Sci. Bull.* **67**, 716–724 (2022).
21. Yang, H. et al. MOF nanosheets as ion carriers for self-optimized zinc anodes. *Energy Environ. Sci.* **16**, 4549–4560 (2023).
22. Yuan, W. et al. Realizing textured zinc metal anodes through regulating electrodeposition current for aqueous zinc batteries. *Angew. Chem.* **135**, e202218386 (2023).
23. Chen, Z. et al. Texture control of commercial Zn foils prolongs their reversibility as aqueous battery anodes. *ACS Energy Lett.* **7**, 3564–3571 (2022).
24. Liu, M. et al. In-situ integration of a hydrophobic and fast-Zn²⁺-conductive inorganic interphase to stabilize Zn metal anodes. *Angew. Chem. Int. Ed.* **62**, e202304444 (2023).
25. Han, J. et al. A thin and uniform fluoride-based artificial interphase for the zinc metal anode enabling reversible Zn/MnO₂ batteries. *ACS Energy Lett.* **6**, 3063–3071 (2021).
26. He, P. & Huang, J. Chemical passivation stabilizes Zn anode. *Adv. Mater.* **34**, 2109872 (2022).
27. Zhang, Q. et al. Revealing the role of crystal orientation of protective layers for stable zinc anode. *Nat. Commun.* **11**, 3961 (2020).
28. Ling, F. et al. Multi-scale structure engineering of ZnSnO₃ for ultra-long-life aqueous zinc-metal batteries. *Adv. Mater.* **35**, 2208764 (2023).
29. Zheng, J. et al. Regulating electrodeposition morphology in high-capacity aluminium and zinc battery anodes using interfacial metal–substrate bonding. *Nat. Energy* **6**, 398–406 (2021).
30. Ji, J. et al. Zinc-contained alloy as a robustly adhered interfacial lattice locking layer for planar and stable zinc electrodeposition. *Adv. Mater.* **35**, 2211961 (2023).
31. Zeng, Y., Pei, Z., Luan, D. & Lou, X. W. D. Atomically dispersed zinophilic sites in N,P-codoped carbon macroporous fibers enable efficient Zn metal anodes. *J. Am. Chem. Soc.* **145**, 12333–12341 (2023).
32. Ma, L. et al. Realizing high zinc reversibility in rechargeable batteries. *Nat. Energy* **5**, 743–749 (2020).
33. Brunklaus, G., Lennartz, P. & Winter, M. Metal electrodes for next-generation rechargeable batteries. *Nat. Rev. Electr. Eng.* **1**, 79–92 (2024).
34. Hobold, G. M. et al. Moving beyond 99.9% Coulombic efficiency for lithium anodes in liquid electrolytes. *Nat. Energy* **6**, 951–960 (2021).
35. Zhu, Y. et al. Concentrated dual-cation electrolyte strategy for aqueous zinc-ion batteries. *Energy Environ. Sci.* **14**, 4463–4473 (2021).
36. Dong, D., Wang, T., Sun, Y., Fan, J. & Lu, Y.-C. Hydrotropic solubilization of zinc acetates for sustainable aqueous battery electrolytes. *Nat. Sustain.* **6**, 1–11 (2023).
37. Pu, S. D. et al. Decoupling, quantifying, and restoring aging-induced Zn-anode losses in rechargeable aqueous zinc batteries. *Joule* **7**, 366–379 (2023).
38. Liu, B., Yuan, X. & Li, Y. Colossal capacity loss during calendar aging of Zn battery chemistries. *ACS Energy Lett.* **8**, 3820–3828 (2023).
39. Liu, Y. et al. Insight into the critical role of exchange current density on electrodeposition behavior of lithium metal. *Adv. Sci.* **8**, 2003301 (2021).
40. Sun, W. et al. A rechargeable zinc-air battery based on zinc peroxide chemistry. *Science* **371**, 46–51 (2021).
41. Wang, W. et al. Regulating interfacial reaction through electrolyte chemistry enables gradient interphase for low-temperature zinc metal batteries. *Nat. Commun.* **14**, 5443 (2023).
42. Zheng, L. et al. Competitive solvation-induced interphases enable highly reversible Zn anodes. *ACS Energy Lett.* **8**, 2086–2096 (2023).
43. Xiong, P. et al. Zn-Ion transporting, in situ formed robust solid electrolyte interphase for stable zinc metal anodes over a wide temperature range. *ACS Energy Lett.* **8**, 1613–1625 (2023).
44. Ma, Y. et al. N,N-dimethylformamide tailors solvent effect to boost Zn anode reversibility in aqueous electrolyte. *Natl Sci. Rev.* **9**, nwac051 (2022).
45. Chang, C. et al. A robust gradient solid electrolyte interphase enables fast Zn dissolution and deposition dynamics. *Energy Environ. Sci.* **17**, 680–694 (2024).
46. Naveed, A., Yang, H., Yang, J., Nuli, Y. & Wang, J. Highly reversible and rechargeable safe Zn batteries based on a triethyl phosphate electrolyte. *Angew. Chem. Int. Ed.* **58**, 2760–2764 (2019).
47. Liu, S. et al. Tuning the electrolyte solvation structure to suppress cathode dissolution, water reactivity, and Zn dendrite growth in zinc-ion batteries. *Adv. Funct. Mater.* **31**, 2104281 (2021).
48. Zhu, J. et al. The construction of binary phase electrolyte interface for highly stable zinc anodes. *Adv. Mater.* **36**, 2304426 (2024).
49. Ni, G. et al. Binary solvents assisting the long-term stability of aqueous K/Zn hybrid batteries. *Mater. Today Energy* **31**, 101204 (2023).
50. Sun, Q. The Raman OH stretching bands of liquid water. *Vib. Spectrosc.* **51**, 213–217 (2009).

Acknowledgements

H.J.F. acknowledges financial support from the Singapore Ministry of Education by Tier 2 (MOE-T2EP50121-0006). W.S. acknowledges the National Natural Science Foundation of China (No. U2330119 and 52302221). H.W. acknowledges the National Natural Science Foundation of China (No. 52272198). Z.W.S. acknowledges the Agency for Science, Technology and Research (MTC Programmatic Fund M23L9b0052 and Central Research Fund Award). The computational work for this article was partially performed on resources of the National Supercomputing Centre, Singapore (<https://www.nscg.sg>). B.Z. acknowledges the University of Electronic Science and Technology of China for startup funding (A1098531023601467). The authors appreciate Tingchuan Zhou and Weijia Ren from Analysis and Testing Center, University of Electronic Science and Technology of China, for technical support. The authors appreciate An Duan and Sha Luo from School of Materials and Energy, University of Electronic Science and Technology of China, for technical support.

Author contributions

H.J.F., H.W. and B.Z. conceived the idea and designed the experiments. B.Z. and J.Y. performed materials characterizations and electrochemical measurements with assistance from J.L., T.X., T.Z., D.C., J.W. Wu, J.Q. Wang, and W.S. C.W. and S.X. conducted XAS measurements. Y.L. and Z.W.S. carried out TOF-SIMS measurements. B.Z. performed the MD simulations and DFT calculations. B.Z., J.Y., W.S., H.W., and H.J.F. co-wrote the paper. All authors discussed the results and commented on the manuscript.

Competing interests

The authors declare no competing interests.

Additional information

Supplementary information The online version contains supplementary material available at <https://doi.org/10.1038/s41467-024-55657-1>.

Correspondence and requests for materials should be addressed to Wei Sun, Houzhao Wan or Hong Jin Fan.

Peer review information *Nature Communications* thanks the anonymous reviewers for their contribution to the peer review of this work. A peer review file is available.

Reprints and permissions information is available at <http://www.nature.com/reprints>

Publisher's note Springer Nature remains neutral with regard to jurisdictional claims in published maps and institutional affiliations.

Open Access This article is licensed under a Creative Commons Attribution-NonCommercial-NoDerivatives 4.0 International License, which permits any non-commercial use, sharing, distribution and reproduction in any medium or format, as long as you give appropriate credit to the original author(s) and the source, provide a link to the Creative Commons licence, and indicate if you modified the licensed material. You do not have permission under this licence to share adapted material derived from this article or parts of it. The images or other third party material in this article are included in the article's Creative Commons licence, unless indicated otherwise in a credit line to the material. If material is not included in the article's Creative Commons licence and your intended use is not permitted by statutory regulation or exceeds the permitted use, you will need to obtain permission directly from the copyright holder. To view a copy of this licence, visit <http://creativecommons.org/licenses/by-nc-nd/4.0/>.

© The Author(s) 2024